

Rate-adaptive Reconciliation for Experimental Continuous-variable Quantum Key Distribution with Discrete Modulation over a Free-space Optical Link

Kadir Gümüř, *Student Member, IEEE*, João dos Reis Frazão, *Student Member, IEEE*, Vincent van Vliet, *Student Member, IEEE*, Sjoerd van der Heide, *Member, IEEE*, Menno van den Hout, *Student Member, IEEE*, Gabriele Liga, *Member, IEEE*, Yunus Can Gültekin, *Member, IEEE*, Aaron Albores-Mejia, *Member, IEEE*, Thomas Bradley, *Member, IEEE*, Alex Alvarado, *Senior Member, IEEE*, and Chigo Okonkwo, *Senior Member, IEEE*

Abstract—Continuous-variable quantum key distribution (CV-QKD) has been proposed as a method for securely exchanging keys to protect against the security concerns caused by potential advancements in quantum computing. In addition to optical fibre transmission, the free-space optical (FSO) channel is an interesting channel for CV-QKD, as it is possible to share keys over this channel wirelessly. The instability of the FSO channel caused by turbulence-induced fading, however, can cause a degradation in the system’s performance. One of the most important aspects of CV-QKD is the reconciliation step, which significantly impacts the performance of the CV-QKD system. Hence, rate-adaptive reconciliation is necessary for CV-QKD over FSO to combat the fluctuations in the channel and improve secret key rates (SKRs). Therefore, in this paper, we simulate the impact of discrete modulation on the reconciliation efficiency and consider the use of d -dimensional reconciliation with $d > 8$ to mitigate this impact, improving reconciliation efficiencies by up to 3.4%. We validate our results by experimentally demonstrating CV-QKD over a turbulent FSO link and demonstrate SKR gains by up to 165%. Furthermore, we optimise the reconciliation efficiency for FSO links, achieving additional SKR gains of up to 7.6%.

Index Terms—Continuous-variable, quantum key distribution, discrete modulation, reconciliation, LDPC codes, free-space optical communication

This work was supported by the Dutch Ministry of Economic Affairs and Climate Policy (EZK), as part of the PhotonDelta National GrowthFunds Programme on Photonics and the QuantumDeltaNL National Growthfunds on Quantum Technology. This article was presented in part at the Optical Fiber Communications (OFC) Conference, San Diego, CA, USA, March 2024 [1]. (*Corresponding author: Kadir Gümüř*)

Kadir Gümüř, João dos Reis Frazão, Vincent van Vliet, Sjoerd van der Heide, Menno van den Hout, Aaron Albores-Mejia, Thomas Bradley, and Chigo Okonkwo are with the High Capacity Optical Transmission Laboratory, Electro-Optical Communications Group, Eindhoven University of Technology, 5600 MB, Eindhoven, The Netherlands. (e-mails: k.gumus@tue.nl, j.c.dos.reis.frazao@tue.nl, v.v.vliet@tue.nl, s.p.v.d.heide@tue.nl, m.v.d.hout@tue.nl, a.albores.mejia@tue.nl, t.d.bradley@tue.nl, cokonkwo@tue.nl)

Aaron Albores-Mejia, Alex Alvarado, and Chigo Okonkwo are with CubiQ Technologies, De Groene Loper 5, Eindhoven, The Netherlands (e-mails: aaron@cubiq-technologies.com, alex@cubiq-technologies.com, chigo@cubiq-technologies.com)

Gabriele Liga, Yunus Can Gültekin, and Alex Alvarado are with the Information and Communication Theory Lab, Signal Processing Group, Eindhoven University of Technology, 5600MB, The Netherlands (e-mails: g.liga@tue.nl, y.c.g.gultekin@tue.nl, a.alvarado@tue.nl)

I. INTRODUCTION

QUANTUM key distribution (QKD), first proposed in [2], has attracted considerable attention in recent years as concerns for information security grow. Using Shor’s algorithm [3], it would be possible to break current public-key cryptography protocols, assuming that sufficiently capable quantum computers can be developed. With continuous advances in quantum computing [4], these concerns are expected to become a reality in the future. A potential solution to these issues is QKD, as it allows for the sharing of secret keys without a potential eavesdropper (Eve) with infinite computational power being able to recover the keys.

QKD can be broadly categorised into two different variants: discrete-variable (DV) [2] and continuous-variable (CV) [5]. DV-QKD involves the transmission of single photons for the distillation of secret keys. Conversely, in CV-QKD, as shown in Fig. 1, quantum random numbers are modulated on the in-phase and quadrature components of coherent light. This light undergoes substantial attenuation to generate weak coherent quantum states. Standard fibre optical telecommunication components can be used for generating and measuring the quantum signal in CV-QKD, which allows for a more cost-effective implementation, as opposed to DV-QKD, which requires single photon detectors [6]. The downside, however, is that post-processing is more challenging for CV-QKD. An important part of the post-processing is the reconciliation, where Alice and Bob try to share bits using error correction. The error correction codes used in CV-QKD are significantly more complex than those used for DV-QKD, and therefore, are the current bottleneck for implementing CV-QKD systems [7].

During reconciliation, the two involved parties, Alice and Bob, use their transmitted and measured quantum states, respectively, to exchange bits for secret key distillation. Alice generates the quantum states using either Gaussian modulation [8], in which she randomly generates a symbol based on a Gaussian distribution or discrete modulation [9], where she uses a finite-size constellation and randomly picks one of the constellation points. Although Gaussian modulation allows for longer distance QKD, practical implementation is difficult, as it is impossible to obtain a perfect Gaussian distribution using electro-optical modulators and digital-to-

analog converters with finite resolution [10]. A system using discrete modulation formats mitigates this issue by approximating Gaussian modulation using probabilistically shaped quadrature amplitude modulation (PS-QAM) [11]. Analysis of different discrete modulation formats for CV-QKD has been performed in, e.g., [12], [13].

A commonly used protocol for reconciliation is multi-dimensional reconciliation, first introduced in [14]. This protocol is especially well-suited for longer-distance CV-QKD systems, as it outperforms slice reconciliation [15], which is mostly used for links of very short distance, in this regime [7]. Low-rate, low-density parity-check (LDPC) codes were designed and simulated for multi-dimensional reconciliation in [16]. In [17], quasi-cyclic LDPC codes were implemented in a graphics processing unit for multi-dimensional reconciliation. Furthermore, in a recent work, real-time error correction for reconciliation was implemented on field programmable gate arrays [18]. An open-source library for the simulation of reconciliation has recently become available in [19].

Another important aspect of reconciliation is the rate-adaptivity, i.e., adapting the rate of the error correction code to match the channel signal-to-noise ratio (SNR). A rate-adaptive version of the multi-dimensional reconciliation protocol was proposed in [20], allowing the CV-QKD system to adapt to the quantum channel fluctuations. This is especially relevant for free-space optical (FSO) channels, as atmospheric turbulence causes changes to the channel over time, resulting in a channel with an unstable SNR [10]. To guarantee good error correction performance, the rate of the code needs to be adapted to match the changes in such a fluctuating channel. The FSO channel can be particularly important for CV-QKD, as it allows for wireless key sharing in cases where a direct fibre link is not possible. An additional review of works on reconciliation can be found in [7].

Experimental demonstrations of CV-QKD, such as over fibre in [21]–[23] and over free-space in [24]–[26] have been performed. However, reconciliation is rarely discussed in detail, and reconciliation efficiencies and frame error rates (FERs) are often assumed. The performance of the reconciliation significantly influences the achievable distances and key rates of these experimental demonstrations. Therefore, we argue that there is a need for more work focusing on reconciliation in experimental demonstrations, as the current literature on reconciliation is mostly theoretical.

Multi-dimensional reconciliation involves the use of multiplications and divisions of ($d = \{1, 2, 4, 8\}$ -) dimensional numbers constructed using the Cayley-Dickson construction [27] in an attempt to construct a virtual channel. The constructed virtual channel is similar to a binary-input additive white Gaussian noise (BI-AWGN) channel. This BI-AWGN channel allows for the design of high-performance error correction codes, which is important as the performance of the error correction greatly affects the achievable secret key rates (SKRs) of CV-QKD [6]. As shown in [28], The higher the dimensionality d of the reconciliation, the more closely the virtual channel resembles a BI-AWGN channel, hence, higher SKRs can be achieved. The dimensionality of reconciliation is often limited to $d = 8$ in literature. This is because

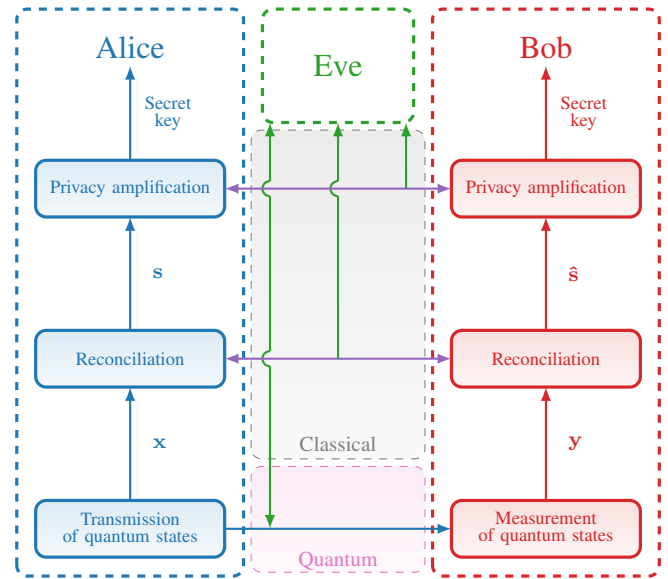


Fig. 1. An overview of a CV-QKD protocol.

the multiplications and divisions used in multi-dimensional reconciliation are only defined for $d = \{1, 2, 4, 8\}$ when constructing such numbers according to the Cayley-Dickson construction [27].

In [14], [16] multi-dimensional reconciliation with $d > 8$, which we will refer to as high-dimensional reconciliation from this point forward, has been proposed and analysed. Instead of using multiplications and divisions, a mapping matrix is used. This high-dimensional reconciliation shows significant gains compared to when $d \leq 8$. This method involves the continuous generation of orthogonal random matrices, which will be used for constructing the mapping matrix. A new mapping matrix needs to be constructed for each set of d symbols for security reasons [14]. However, recent works have not investigated further methods for high-dimensional reconciliation, and we conjecture that this is because of the higher complexity of the protocol caused by the generation of the orthogonal matrices. Additionally, to the best of our knowledge, no analysis on high-dimensional reconciliation for discrete modulation formats for different code rates has been performed.

In this work, we investigate how the use of discrete modulation formats impacts the performance of error correction over a wide range of code rates. We consider the use of high-dimensional reconciliation to improve the reconciliation efficiency, showing improvements in reconciliation efficiencies, especially for short- and mid-range CV-QKD systems, by up to 3.4%. Furthermore, we experimentally demonstrate high-dimensional reconciliation with CV-QKD transmission over a turbulent FSO channel with varying turbulence strengths and show that we can increase SKRs by up to 165% compared to conventional multi-dimensional reconciliation. Finally, we show how optimising the reconciliation efficiency to take into account the fluctuations in optical power induced by fading in the FSO channel allows for an additional 7.6% gain in SKR.

The remainder of the paper is organised as follows. In

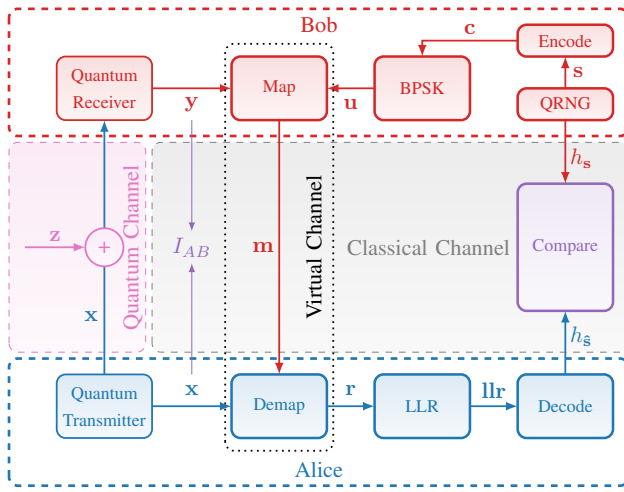


Fig. 2. An overview of the reverse multi-dimensional reconciliation protocol for CV-QKD.

Section II, we discuss the multi-dimensional reconciliation conventionally used in CV-QKD systems. Section III expands on this by explaining the high-dimensional reconciliation and shows how the dimensionality of the reconciliation affects the error correction performance for different discrete modulation formats. Section IV explains the idea of rate-adaptivity and how it influences the error correction performance. Our results are experimentally validated in Section V. Finally, in Section VI, we conclude our work and give suggestions for potential future research.

II. MULTI-DIMENSIONAL RECONCILIATION

In a conventional CV-QKD protocol, reconciliation takes place after the transmission and measurement of the quantum states. During reconciliation, Alice and Bob try to securely exchange a string of bits, which will be used for the secret key distillation in the privacy amplification step. The most common form is reverse reconciliation where the algorithm terminates at the transmitter side Alice. This achieves longer distances when compared to direct reconciliation, which is affected by the so-called 3 dB limit [6]. An overview of reverse reconciliation is given in Fig. 2, and described in what follows.

The multi-dimensional reconciliation we will describe in this section involves the use of high dimensional numbers and is only defined for $d \in \{1 \text{ (real)}, 2 \text{ (complex)}, 4 \text{ (quaternion)}, 8 \text{ (octonion)}\}$ [14]. All of the multiplications and divisions between vectors of length d in the rest of this section correspond to those between two d -dimensional numbers.

At the start of reconciliation, Alice and Bob have their transmitted and measured coherent quantum states, \mathbf{x} and \mathbf{y} , respectively. Here, $\mathbf{x} = [x_1^I, x_1^Q, x_2^I, \dots, x_{N/2}^Q]$, is a sequence of real symbols of length N , randomly chosen from a constellation \mathcal{X} according to the probabilities assigned during probabilistic shaping, where I and Q refer to the in-phase and quadrature components of the constellation, and

$$\mathbf{y} = \mathbf{x} + \mathbf{z}, \quad (1)$$

where $\mathbf{z} = [z_1^I, z_1^Q, z_2^I, \dots, z_{N/2}^Q]$ are independent and identically distributed Gaussian noise samples with zero mean and variance $\sigma_z^2/2$. In this work, we assume that $\mathbb{E}[|x_i^I|^2 + |x_i^Q|^2] = 1$ with $\mathbb{E}[|x_i^I|^2] = \mathbb{E}[|x_i^Q|^2] = \frac{1}{2}$, i.e., the variance of a quantum state is 1. The signal-to-noise ratio (SNR) of the quantum channel is thus defined to be $1/\sigma_z^2$. For the rest of the paper, we will use the notation $\mathbf{x} = [x_1, x_2, \dots, x_N]$ where $[x_{2i-1}, x_{2i}] = [x_i^I, x_i^Q] \quad \forall i \in 1, 2, \dots, N/2$. The same notation will be used as well for \mathbf{y} and \mathbf{z} .

Using a quantum random number generator (QRNG), Bob generates a string of bits $\mathbf{s} = [s_1, s_2, \dots, s_K]$ of length K , which are the information bits that will be used for key distillation. Bob encodes these bits into a codeword $\mathbf{c} = [c_1, c_2, \dots, c_N]$ using a rate $R = K/N$ error correction code. The bits in \mathbf{c} are then converted to binary phase-shift keying (BPSK) symbols \mathbf{u} using $u_i = (-1)^{c_i}$.

We split \mathbf{u} , \mathbf{y} , and \mathbf{x} into N/d vectors of length d , $\mathbf{u}'_j = [u_{d \cdot j - d + 1}, u_{d \cdot j - d + 2}, \dots, u_{d \cdot j}]$, $\mathbf{y}'_j = [y_{d \cdot j - d + 1}, y_{d \cdot j - d + 2}, \dots, y_{d \cdot j}]$, and $\mathbf{x}'_j = [x_{d \cdot j - d + 1}, x_{d \cdot j - d + 2}, \dots, x_{d \cdot j}] \quad \forall j = 1, 2, \dots, N/d$. Here, N is assumed to be divisible by d . Each new vector of length d corresponds to a d -dimensional number. Bob calculates \mathbf{m}'_j using

$$\mathbf{m}'_j = \mathbf{u}'_j \mathbf{y}'_j, \quad \forall j \in 1, 2, \dots, N/d, \quad (2)$$

and communicates $\mathbf{m} = [\mathbf{m}'_1, \mathbf{m}'_2, \dots, \mathbf{m}'_{N/d}]$ to Alice over the classical authentication channel, which is assumed to be error-free. Eve has full access to the classical authentication channel and can obtain any information that is transmitted over that channel.

To recover \mathbf{u} from \mathbf{m} , Alice divides \mathbf{m} by her transmitted states \mathbf{x}

$$\mathbf{r}'_j = \frac{\mathbf{m}'_j}{\mathbf{x}'_j} \quad \forall j \in 1, 2, \dots, N/d. \quad (3)$$

Doing the multiplication in (2) and division in (3) creates a virtual channel closely resembling a BI-AWGN channel. The BI-AWGN channel is a frequently-used model for the design of capacity-approaching error correction code design, i.e., with a high reconciliation efficiency β . From (1) and (3), we write that

$$\begin{aligned} \mathbf{r}'_j &= \frac{\mathbf{m}'_j}{\mathbf{x}'_j} = \frac{\mathbf{u}'_j \mathbf{y}'_j}{\mathbf{x}'_j} \\ &= \frac{\mathbf{u}'_j (\mathbf{x}'_j + \mathbf{z}'_j)}{\mathbf{x}'_j} \\ &= \mathbf{u}'_j + \frac{\mathbf{u}'_j \mathbf{z}'_j}{\mathbf{x}'_j}. \end{aligned} \quad (4)$$

Because \mathbf{y} is a noisy version of \mathbf{x} , Alice is left with the original BPSK symbols \mathbf{u}'_j , but with additive noise $\mathbf{n}'_j = \frac{\mathbf{u}'_j \mathbf{z}'_j}{\mathbf{x}'_j}$. We also define $\mathbf{n} = [\mathbf{n}'_1, \mathbf{n}'_2, \dots, \mathbf{n}'_{N/d}]$.

We show the noise distribution of the virtual channel in (4) in the following. We will consider the case where $d = 1$, in which case $\mathbf{n}'_j = \frac{u'_j z'_j}{x'_j}$. The random variables are all i.i.d. and therefore do not depend on j , hence for the probability

distributions we will remove the subscript j . As mentioned before, the noise distribution of z' is:

$$f(z') = \mathcal{N}\left(0, \frac{\sigma_z^2}{2}\right), \quad (5)$$

as the source of the noise is the quantum channel, which is assumed to be AWGN with noise variance $\sigma_z^2/2$ per quadrature. Because Alice knows the value of x' , the probability distribution of n' , conditioned on x' , is:

$$f(n'|x') = \mathcal{N}\left(0, \frac{\sigma_z^2}{2|x'^2|}\right), \quad (6)$$

as the probability distribution does not depend on u' , i.e., $f(n'|x', u' = 1) = f(n'|x', u' = -1)$. Alice, therefore, observes a channel where each channel use j has a different SNR, which is dependent on x'^2 . In [17] it is shown that this result generalises for $d = \{2, 4, 8\}$ to

$$f(\mathbf{n}'|\mathbf{x}') = \mathcal{N}\left(\mathbf{0}, \mathbf{I}_d \frac{d\sigma_z^2}{2\|\mathbf{x}'\|^2}\right), \quad (7)$$

where \mathbf{I}_d is a $d \times d$ identity matrix. Hence, the noise variance σ_j^2 for each set of d received symbols is different for each block of j symbols and is dependent on \mathbf{x}'_j via

$$\sigma_j^2 = \frac{d\sigma_z^2}{2\|\mathbf{x}'_j\|^2}. \quad (8)$$

Alice calculates the log-likelihood ratios (LLRs) of her message \mathbf{r}'_j [17]

$$\text{llr}'_j = \frac{2\mathbf{r}'_j}{\sigma_j^2}. \quad (9)$$

Using $\text{llr} = [\text{llr}'_1, \text{llr}'_2, \dots, \text{llr}'_{N/d}]$, Alice attempts to decode the codeword to estimate the information bits $\hat{\mathbf{s}}$.

As mentioned before, the virtual channel has a different noise variance for each block of d symbols. The distribution of the noise, therefore, does not correspond to that of a BI-AWGN channel where each channel use has the same noise variance. The distribution of n , where n is a value randomly sampled from \mathbf{n} , is not Gaussian, as shown in Fig. 3 for $d = 1$ and $d = 8$. For $d = 1$, the distribution of n is wider and less Gaussian compared to $d = 8$. The noise distribution more closely resembles that of a fading channel [29], which

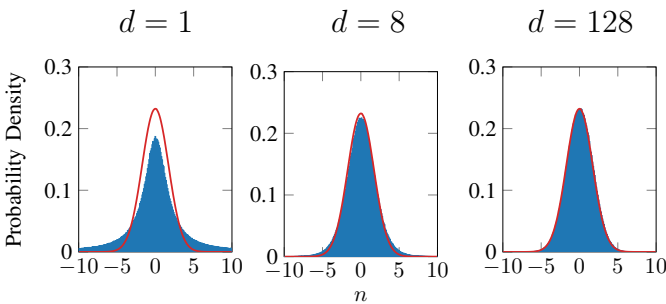


Fig. 3. The histograms of n for different d assuming Gaussian modulation for \mathbf{x} with 10^6 samples at an SNR of -4.7 dB. The red line corresponds to the probability density function of n for a BI-AWGN channel with the same SNR.

is because of fluctuations in σ_j^2 . The capacity of the fading channel is lower compared to an AWGN channel with the same average SNR, hence the capacity of the virtual channel is lower than the quantum channel. As a result, the reconciliation efficiency suffers as the error correction codes are applied to a channel with lower capacity, i.e., the code rate decreases.

For the virtual channel to be BI-AWGN, we can use a modulation format where each symbol has equal power (such as quadrature phase-shift keying (QPSK)), such that σ_j^2 is constant as $\|\mathbf{x}'_j\|^2$ is always the same for QPSK. For other modulation formats, we can increase d because of the following: let $\|\mathbf{x}'_j\|^2 = \sum_{i=1}^d \|x_{j-d+i}\|^2$, where $\|x_{j-d+i}\|^2$ is i.i.d. with mean $\mu_{\|x\|^2}$ and variance $\sigma_{\|x\|^2}^2$, which are both finite. The law of large numbers [30] states that if we sample and sum d independent random samples from an i.i.d. process, the sum will converge to $d\mu$ as $d \rightarrow \infty$, and the variance of the sum will be equal to $\frac{\sigma^2}{d}$. Therefore, because $\sigma_{\|x\|^2}^2$ is finite, $\text{Var}(\|\mathbf{x}'\|^2) \rightarrow 0$, and consequently $\text{Var}(\sigma_j^2) \rightarrow 0$, when $d \rightarrow \infty$. This means that σ_j^2 will have the same value for each j when d is infinite. By increasing d , we are effectively reducing the amount of fading in the channel as we are reducing the variance of $\|\mathbf{x}'\|^2$. Note that QPSK modulation heavily limits the transmission distance for CV-QKD systems when compared to PS-QAM or Gaussian modulation [10]. Therefore, using higher dimensional reconciliation is necessary, which will be discussed in the next section.

Because of the relatively high FERs used in CV-QKD systems, the probability of a miscorrection on Alice's side is quite high. Therefore, after decoding, Alice and Bob confirm that \mathbf{s} and $\hat{\mathbf{s}}$ are the same using a cyclic redundancy check (CRC). Although it is still possible that $\mathbf{s} \neq \hat{\mathbf{s}}$ after the CRC, it can be shown that the probability of this happening is close to 0 [17]. If the decoding is successful, the bits will be used during privacy amplification to distil the secret key, otherwise, a frame error has occurred and the frame will be discarded.

The SKR for a CV-QKD protocol using multi-dimensional reconciliation depends on both the rate of the code and the frame error rate (FER) via [14]

$$\text{SKR} = (1 - \text{FER})(\beta I_{AB} - \chi_{BE} - \Delta), \quad (10)$$

where $\beta = \frac{R}{I_{AB}}$ is the reconciliation efficiency, I_{AB} is the mutual information between Alice's transmitted and Bob's measured quantum states, χ_{BE} is the Holevo information between Bob's and Eve's measurements, and Δ is the penalty caused by the finite size effects of the privacy amplification [17]. We calculate Δ using:

$$\Delta = 7\sqrt{\frac{\log_2(2/\epsilon)}{N_{\text{privacy}}}}, \quad (11)$$

where ϵ is the security parameter, which was chosen to be 10^{-10} [31], and N_{privacy} is the privacy amplification block size. There is a trade-off between β and FER, as the FER increases when β increases, as we are operating with a code rate closer to capacity [32]. The optimum SKR is often achieved at a FER around 10-30% [7].

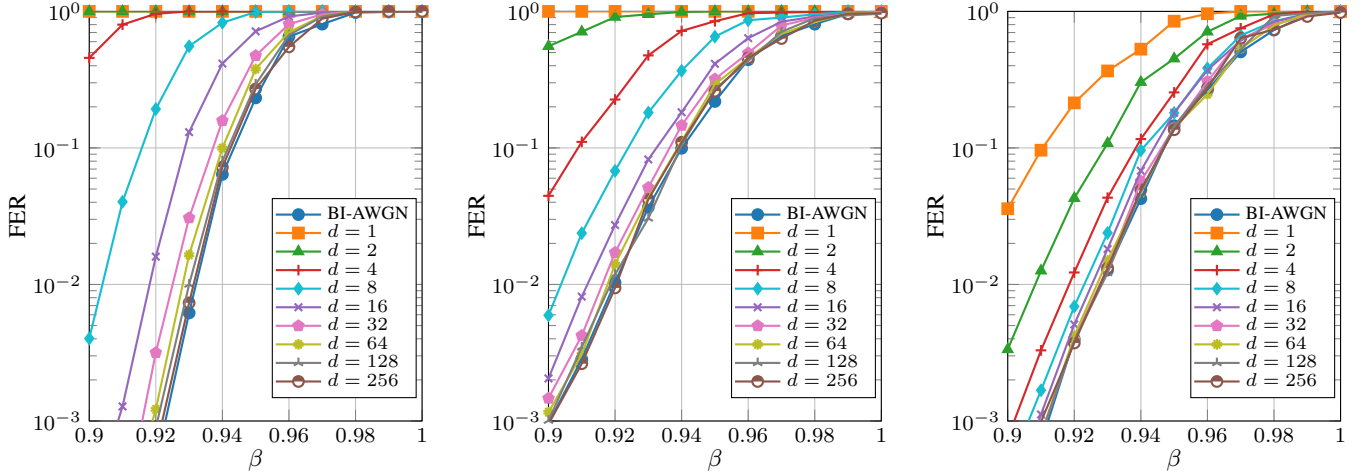


Fig. 4. Simulated FER vs. β for different rate (Left: $R = \frac{1}{5}$, Middle: $R = \frac{1}{10}$, Right: $R = \frac{1}{50}$) TPB-LDPC codes for different d .

III. HIGH-DIMENSIONAL RECONCILIATION

Instead of using multiplication and division during the construction of the virtual channel, it is possible to go beyond $d = 8$ for the multi-dimensional reconciliation using a different construction as proposed in [14]. We will refer to multi-dimensional reconciliation with $d > 8$ as high-dimensional reconciliation in the rest of this section. We will use a $d \times d$ mapping matrix \mathbf{R}_j which maps \mathbf{y}'_j to \mathbf{u}'_j :

$$\mathbf{R}_j \mathbf{y}'_j = \mathbf{u}'_j. \quad (12)$$

This mapping matrix can be transmitted over the channel without leaking any information as \mathbf{R}_j and \mathbf{u}'_j are statistically independent if \mathbf{R}_j is constructed in the following manner [14].

First, we generate a random orthogonal $d \times d$ matrix \mathbf{Q}_j according to the Haar measure [33]. This can be done by taking the orthogonal part of the QR decomposition of a normalised random Gaussian matrix. The generation of \mathbf{Q}_j in this way has complexity $\mathcal{O}(d^3)$, but a simplified method exists with complexity $\mathcal{O}(d^2)$ as described in [16]. The complexity of high-dimensional reconciliation is dominated by the generation of \mathbf{Q}_j . \mathbf{Q}_j must be randomly generated for each j to prevent information leakage [16]. In this paper, for simulation purposes, for each codeword, only one \mathbf{Q} gets generated and used for each \mathbf{Q}_j to simplify the simulation.

We then create a Householder matrix [34] \mathbf{S}_j between \mathbf{u}'_j and $\mathbf{Q}_j \mathbf{y}'_j$

$$\mathbf{S}_j = \mathbf{I}_d - 2 \frac{\mathbf{a}_j \mathbf{a}_j^T}{\|\mathbf{a}_j\|^2}, \quad (13)$$

where

$$\mathbf{a}_j = \mathbf{Q}_j \mathbf{y}'_j - \mathbf{u}'_j \sqrt{\frac{\|\mathbf{y}'_j\|^2}{d}}. \quad (14)$$

We scale \mathbf{u}'_j by $\sqrt{\frac{\|\mathbf{y}'_j\|^2}{d}}$ so that the hyperplane between this vector and $\mathbf{Q}_j \mathbf{y}'_j$ goes through the origin, as this is a requirement for creating a Householder matrix [34]. By doing this, we now map \mathbf{y}'_j to $\mathbf{u}'_j \sqrt{\frac{\|\mathbf{y}'_j\|^2}{d}}$ instead of \mathbf{u}'_j . This scaling

factor will be taken into account during the LLR calculations. We can then calculate \mathbf{R}_j as

$$\mathbf{R}_j = \mathbf{S}_j \mathbf{Q}_j. \quad (15)$$

The resulting mapping matrix \mathbf{R}_j is orthogonal, as it is a multiplication of two orthogonal matrices. Bob then transmits \mathbf{R}_j to Alice over the classical channel along with $\|\mathbf{y}'_j\|^2$.

Alice attempts to reconstruct \mathbf{u}'_j by applying the mapping matrix \mathbf{R}_j to \mathbf{x}'_j

$$\begin{aligned} \mathbf{R}_j \mathbf{x}'_j &= \mathbf{R}_j (\mathbf{y}'_j - \mathbf{z}'_j) \\ &= \mathbf{R}_j \mathbf{y}'_j - \mathbf{R}_j \mathbf{z}'_j \\ &= \mathbf{u}'_j \sqrt{\frac{\|\mathbf{y}'_j\|^2}{d}} - \mathbf{R}_j \mathbf{z}'_j. \end{aligned} \quad (16)$$

Because \mathbf{y}'_j is a noisy version of \mathbf{x}'_j , \mathbf{R}_j will map \mathbf{x}'_j to a point close to $\mathbf{u}'_j \sqrt{\frac{\|\mathbf{y}'_j\|^2}{d}}$. Hence, after applying \mathbf{R}_j to \mathbf{x}'_j , Alice will have $\mathbf{u}'_j \sqrt{\frac{\|\mathbf{y}'_j\|^2}{d}}$ with additive noise $\mathbf{n}'_j = -\mathbf{R}_j \mathbf{z}'_j$. The probability distribution of \mathbf{n}'_j given \mathbf{R}_j is known to Alice, can be determined as follows. Consider the probability distribution of \mathbf{z}' :

$$f(\mathbf{z}') = \mathcal{N}\left(\mathbf{0}, \mathbf{I}_d \frac{\sigma_z^2}{2}\right). \quad (17)$$

Multiplying \mathbf{z}' by \mathbf{R} , where \mathbf{R} is an instance of \mathbf{R}_j , does not change the mean value of the distribution, as

$$\mathbb{E}[-\mathbf{R}\mathbf{z}'] = -\mathbf{R}\mathbb{E}[\mathbf{z}'] = -\mathbf{R}\mu_{\mathbf{z}'} = \mathbf{0}. \quad (18)$$

The covariance matrix of $\mathbf{R}\mathbf{z}'$ is then:

$$\begin{aligned} \text{cov}(-\mathbf{R}\mathbf{z}') &= \mathbb{E}[(-\mathbf{R}\mathbf{z}')(-\mathbf{R}\mathbf{z}')^T] \\ &= \mathbf{R}\mathbb{E}[\mathbf{z}'\mathbf{z}'^T]\mathbf{R}^T \\ &= \frac{\sigma_z^2}{2} \mathbf{R}\mathbf{I}_d\mathbf{R}^T \\ &= \frac{\sigma_z^2}{2} \mathbf{I}_d, \end{aligned} \quad (19)$$

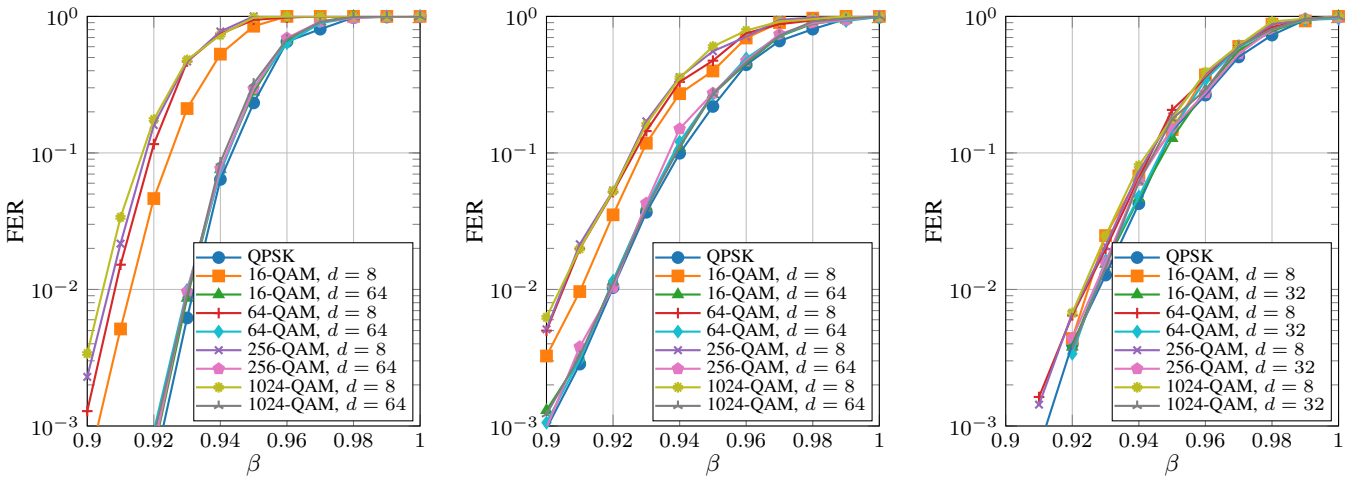


Fig. 5. Simulated FER vs. β for different rate (Left: $R = \frac{1}{5}$, Middle: $R = \frac{1}{10}$, Right: $R = \frac{1}{50}$) TPB-LDPC codes for different d and modulation formats.

because \mathbf{R} is an orthogonal matrix, hence $\mathbf{R}\mathbf{R}^T = \mathbf{I}_d$. Therefore, the probability distribution of \mathbf{n}' is:

$$f(\mathbf{n}'|\mathbf{R}) = \mathcal{N}\left(\mathbf{0}, \mathbf{I}_d \frac{\sigma_z^2}{2}\right). \quad (20)$$

Once again, this distribution is i.i.d., and therefore independent of j . For each block of j symbols, we have created a BI-AWGN channel with signal power $\frac{\|\mathbf{y}'_j\|^2}{d}$ and noise variance $\sigma_z^2/2$. Alice can then calculate llr'_j

$$\text{llr}'_j = 2 \frac{\mathbf{R}_j \mathbf{x}'_j}{\sigma_j^2}, \quad (21)$$

where

$$\sigma_j^2 = \frac{\sigma_z^2}{2} \sqrt{\frac{d}{\|\mathbf{y}'_j\|^2}}, \quad (22)$$

and use these LLRs for the decoding.

To compare the noise distribution of high-dimensional reconciliation to multi-dimensional reconciliation with $d \leq 8$, we define \mathbf{n} for high-dimensional reconciliation as $\mathbf{n} = [\mathbf{n}'_1/(\|\mathbf{y}'_1\|^2/d), \mathbf{n}'_2/(\|\mathbf{y}'_2\|^2/d), \dots, \mathbf{n}'_{N/d}/(\|\mathbf{y}'_{N/d}\|^2/d)]$, i.e., we normalise the noise such that the signal power for each j is equal 1. The virtual channel approaches a BI-AWGN with noise variance $\sigma_z^2/2$, which is shown in Fig. 3 where the histogram of n when $d = 128$ follows a Gaussian probability density function almost exactly. We can once again use the law of large numbers [30] to show why increasing d causes to virtual channel to approach the BI-AWGN channel. Let $\|\mathbf{y}'_j\|^2 = \sum_{i=1}^d \|y_{j-d+i}\|^2$, where $\|y_{j-d+i}\|^2$ is i.i.d. with mean $\mu_{\|y\|^2}$ and variance $\sigma_{\|y\|^2}^2$, which are also both finite. Because $\|\mathbf{y}'_j\|^2$ is a sum of i.i.d. random variables with a finite mean and variance, $\text{Var}(\|\mathbf{y}'_j\|^2) \rightarrow 0$ as $d \rightarrow \infty$, hence the signal power $\frac{\|\mathbf{y}'_j\|^2}{d}$ is the same for each j .

To analyse the effect of the multi-dimensional reconciliation on the performance of the error correction, we have simulated the FER curves for three different rate type-based protograph (TBP) LDPC codes ($R = \frac{1}{5}$, $R = \frac{1}{10}$, $R = \frac{1}{50}$) [35] corresponding to short-, mid-, and long-range CV-QKD links for a large range of values of d . The quasi-cyclic parity check

matrices for these codes were generated using progressive edge-growth with the approximate cycle extrinsic message degree constraint [36], with cyclant sizes of 200, 200, and 500, and N of 10^5 , 10^5 , and 10^6 respectively. Gaussian modulation was used to generate the quantum states. The maximum amount of decoding iterations was set to 500, and for each data point, we simulated until at least 100 frame errors occurred or a maximum of 10^5 frames had been simulated with the all-zero codeword assumption.

The results of these simulations are shown in Fig. 4. The performance of these simulations depends on both d and R . For $R = \frac{1}{5}$, there is a significant gap in performance between $d = 8$ and $d = 128$, namely 2.7% β for an FER of 10%. When the rate of the code decreases, this gap diminishes, with a 1.6% difference for $R = \frac{1}{10}$, and 0.5% for $R = \frac{1}{50}$. We conjecture that this is because in the lower SNR regime the decrease in channel capacity of the virtual channel compared to the quantum channel, caused by using a finite d in multi-dimensional reconciliation, is smaller. It is still worth considering using high-dimensional reconciliation for long-distance CV-QKD links. Even though the complexity increases by more than an order of magnitude when using $d = 128$ compared to $d = 8$, this remains negligible compared to the complexity of the decoding while offering an increase in β . However, it is mostly useful for short to mid-distance links, as this increase in β can lead to significant increases in SKR, as will be shown later.

We also simulated how different modulation formats impact the multi-dimensional reconciliation. The modulation formats are PS-QAM constellations, designed according to [12]. As shown in Fig. 5, the modulation format has a slight impact on the error correction performance. QPSK modulation performs the best because all symbols have equal power, and therefore, the virtual channel created during reconciliation corresponds to a BI-AWGN channel regardless of what d is. When increasing the cardinality of the constellation, the performance of the error correction code worsens when $d = 8$, as the amount of different power levels in the constellation increases, hence the noise variance of each channel use varies more. This is especially clear for $R = \frac{1}{5}$, but for $R = \frac{1}{10}$ and

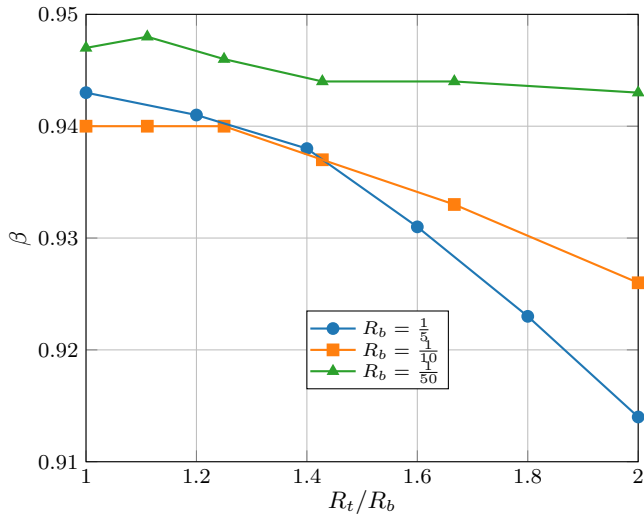


Fig. 6. Simulated results. The β at which an FER of 10% is achieved vs. the relative rate of the punctured code for TBP-LDPC codes.

$R = \frac{1}{50}$ the modulation formats are closer in performance. When we choose a high d , the error correction curves almost completely overlap for all of the codes for the different modulation formats.

IV. RATE ADAPTIVITY

As mentioned before, rate adaptivity is an important part of reconciliation, as fluctuations in the quantum channel can cause the values of I_{AB} and χ_{BE} , which are estimated during the parameter estimation, to change. To operate at a steady β , the rate of the code needs to be changed to match βI_{AB} . We achieve this rate adaptivity using puncturing as described in the sp -protocol proposed in [20]. Using this protocol, it is possible to obtain a wide range of code rates without needing multiple LDPC codes designs.

At the start of reconciliation, Bob knows both I_{AB} from the parameter estimation, and the target β , and has an LDPC code with base rate R_b . Bob calculates the target code rate R_t , which should be larger than R_b as with puncturing, it is only possible to increase the rate of the code. Bob determines the amount of bits that need to be punctured p :

$$p = \left\lfloor N - \frac{R_b N}{R_t} \right\rfloor, \quad (23)$$

where we use the floor operation as p has to be an integer. Bob then randomly generates a vector $\mathbf{w} = [w_1, w_2, \dots, w_p]$,

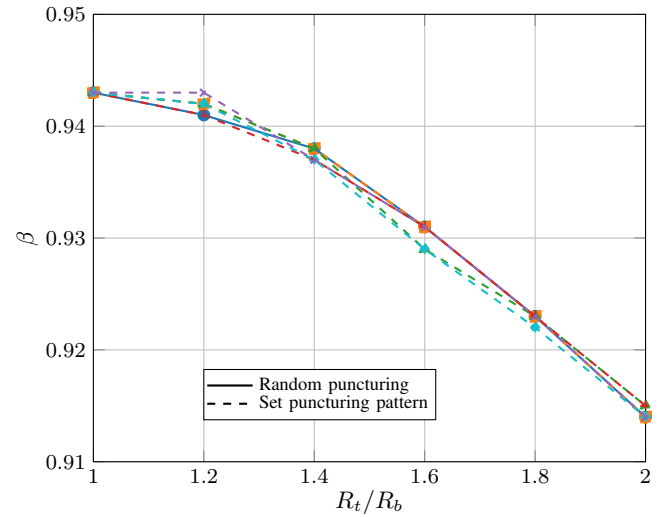


Fig. 7. Simulated results. The β at which an FER of 10% is achieved vs the relative rate of the punctured code for a $R = \frac{1}{5}$ TBP-LDPC code, comparing random puncturing with a set puncturing pattern. For the simulations, 5 different set puncturing patterns were simulated.

where each value w_i is a unique integer with a value between 1 and N , indicating the position of the punctured bits in the codeword. When calculating \mathbf{m} , Bob does not calculate a message for these specific bit positions, i.e., \mathbf{m} will have a length of $N - p$. Bob transmits \mathbf{w} alongside \mathbf{m} . During decoding, Alice will set the LLRs of the punctured bits to 0.

We have simulated the performance of the puncturing for three different codes, the same $R_b = \frac{1}{5}$, $R_b = \frac{1}{10}$, and $R_b = \frac{1}{50}$ TBP-LDPC codes used in Fig. 4 and 5. We have randomly punctured the codes for a wide range of code rates, up until twice the base code rate. Figure 6 shows at which β an FER of 10% is achieved for the different codes and rates, which we have determined from the β vs. FER curves obtained during the simulation. For $R_b = \frac{1}{5}$, the error correction performance drops over a wide range of code rates, when doubling the rate there is a 2.9% penalty in β . When R_b decreases, we can see that the codes become more resilient to rate changes, as for the $R_b = \frac{1}{50}$ code the error correction performance stays almost constant when increasing the rate.

Instead of randomly generating and transmitting \mathbf{w} every single time, it is also possible to generate a set puncturing pattern $\mathbf{v} = [v_1, v_2, \dots, v_N]$, which is a random scrambling of all integers from 1 to N . This puncturing pattern is known to all parties. Bob then only needs to transmit p over the channel, indicating that bits v_1 to v_p are punctured. This simplifies the puncturing process, as Bob does not need to generate and

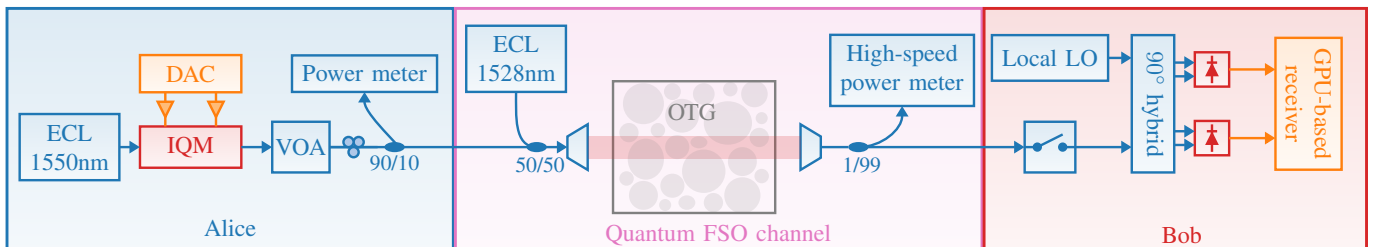


Fig. 8. The CV-QKD setup for transmission over an FSO channel with an optical turbulence generator.

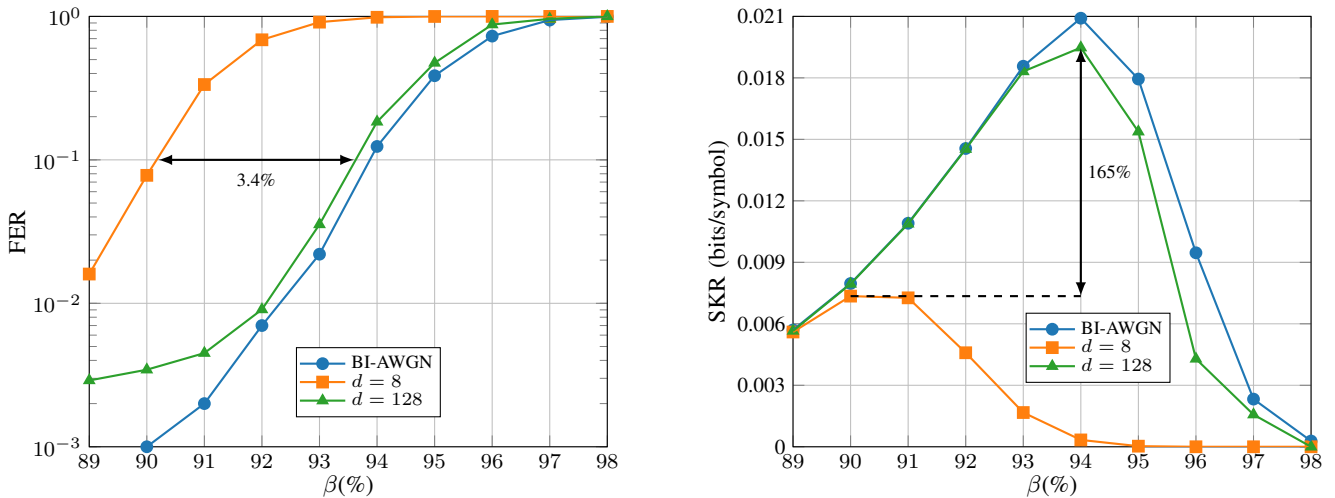


Fig. 9. Experimental results. Left: The FER of the $R = \frac{1}{5}$ expanded TBP-LDPC code when punctured to $R = 0.3$ for different d compared to the BI-AWGN channel. Right: The SKR of the $R = \frac{1}{5}$ expanded TBP-LDPC code when punctured to $R = 0.3$ for different d compared to the BI-AWGN channel for the FSO channel with $\sigma_I = 0.001$ and $\beta_{jitter} = 123.8$.

transmit w every single frame.

We have simulated the puncturing for five different \mathbf{v} , which were all randomly generated, and compared it to random puncturing for the $R = \frac{1}{5}$ TBP-LDPC code with $N = 10^5$. Figure 7 shows that using a set puncturing pattern has little influence on the error correction performance compared to generating a random puncturing pattern every frame. It should be noted that it is possible to optimise \mathbf{v} for a specific code to improve the puncturing performance [37], however, that is outside of the scope of this paper.

Until now, we have assumed that β has a constant value during reconciliation. When there are fluctuations in the quantum channel, the rate of the code is changed to obtain this β . This β is chosen to optimise the SKR of the system, assuming that the parameters of the system, such as the excess noise, are constant. This approach is valid for CV-QKD transmission over fibre, as the fibre channel is stable. However, factors such as atmospheric turbulence cause additional time-dependent instabilities in FSO channels. Hence, the optimal β changes over time. During the parameters estimation, Bob continuously determines I_{AB} and χ_{BE} of the measured quantum symbols during the parameter estimation. Bob does this on a per-block basis, where Bob measures N_p quantum symbols and does the parameter estimation over this entire CV-QKD block. For each CV-QKD block, β can be optimised. This can be simply implemented by using a β -FER look-up table, and calculating which β -FER pair optimises the SKR for a specific block. This adds a negligible amount of increase in the complexity of the parameter estimation. In the next section, we show how β -optimisation can increase the SKR.

V. EXPERIMENTAL SETUP

Fig. 8 shows the experimental setup employed for CV-QKD transmission validation over a free-space optical (FSO) channel. On Alice's side, we deploy a <100 kHz linewidth external cavity laser (ECL) tuned to 1550 nm (this is similar to the linewidth of lasers in commercial transceivers), a digital-to-analogue (DAC) converter, and an optical IQ-modulator

(IQM) to transmit a PS-256QAM constellation with a symbol rate of 250 MBaud. A variable optical attenuator (VOA) and a power meter are used to attenuate the signal to an average power of 7.44 shot noise units (SNU) (-69.2 dBm). We combine a second tone produced by a second ECL for turbulence characterisation placed at 1528 nm with the attenuated 1550 nm quantum signal and coupled to free space using a collimator. The light then traverses an optical turbulence generator (OTG) [38], [39], which can mimic FSO channels with various turbulence strengths. We split off 1% of the light to a high-speed power meter for FSO channel characterisation. For our setup, we have measured four different turbulence strengths generated by the OTG with scintillation indices $\sigma_I = 0.001, 0.009, 0.01, 0.013$ and pointing jitter $\beta_{jitter} = 123.8, 8.6, 3.0, 1.6$ respectively, which would all be classified as weak fluctuations, corresponding to calm weather conditions [40].

The remaining 99% of light is directed to Bob's side, where for the 90° optical hybrid, a local ECL is used as a local local oscillator (LLO), after which the outputs are digitised. Note that a single polarisation optical setup was used for this experiment. Polarisation is aligned beforehand using a polarisation controller and is stable during measurements. Calibration and recovery of the quantum signal is done using digital signal processing [41]. During the parameter estimation, I_{AB} , the excess noise ξ_{Bob} , and χ_{BE} are estimated, taking into account finite-size effects [42]. Relevant parameters for the system are a quantum efficiency of 40%, $N_{privacy} = 6.8 \cdot 10^6$, a clearance of 10 dB, an average ξ_{Bob} of 0.0045 SNU, and an average transmittance T of 0.41.

We use 128-dimensional reconciliation. Furthermore, we use the $R = 0.2$ expanded TBP-LDPC code punctured to $R \approx 0.3$, around the average I_{AB} of the system, for error correction. We choose a block length $N = 1.024 \cdot 10^5$ with a maximum of 500 decoding iterations. We have also implemented the β -optimisation as well.

Figure 9 shows both the FER (left) and the SKR (right)

of the experimental results for the case when $\sigma_I = 0.001$ and $\beta_{jitter} = 123.8$ assuming a constant β for all CV-QKD blocks. As expected, the FER of the 128-dimensional reconciliation is close in performance to the BI-AWGN, and at an FER of 10% there is an increase in β of approximately 3.4% compared to the 8-dimensional case. This is slightly more gain compared to the results in Fig. 5 because of the higher code rate. As a result, the SKR sees an increase of 165%, where the optimal SKR is achieved at $\beta = 94\%$.

In Fig. 10 we show how I_{AB} and χ_{BE} and the optimal β changes over time for the FSO transmission with $\sigma_I = 0.009$, $\beta_{jitter} = 8.6$, and $N_p = 10^7$. We have transmitted a total of 120 CV-QKD blocks. We can see from the figure that I_{AB} fluctuates slightly over time, while for χ_{BE} , the fluctuations are more significant. This is because the fluctuations are mainly caused by fluctuations in ξ_{bob} , which has a larger influence on χ_{BE} than on I_{AB} [6]. For the reconciliation, the optimal β for most CV-QKD blocks tends to be close to the previously mentioned 94%. For some CV-QKD block the optimal β is much higher, because the gap between I_{AB} and χ_{BE} is much smaller, hence a higher β is required to get a positive SKR. There are also some CV-QKD blocks where reconciliation is not possible, as indicated by the red crosses. In these cases, χ_{BE} is either very close to or even larger than I_{AB} , and for positive SKRs, the required β is not achievable with our error correction code.

The effects of both the β -optimisation and the different turbulence settings on the overall SKR of the system are shown in Fig. 11. For all turbulence settings, the optimal SKR without β -optimisation, i.e., when β is chosen to be the same for each CV-QKD block, is achieved at $\beta = 94\%$. The overall SKR of the system decreases when the turbulence increases, however, three of the turbulence settings are very close in performance to each other, as for these settings the turbulence strength is similar. When applying β -optimisation, gains of

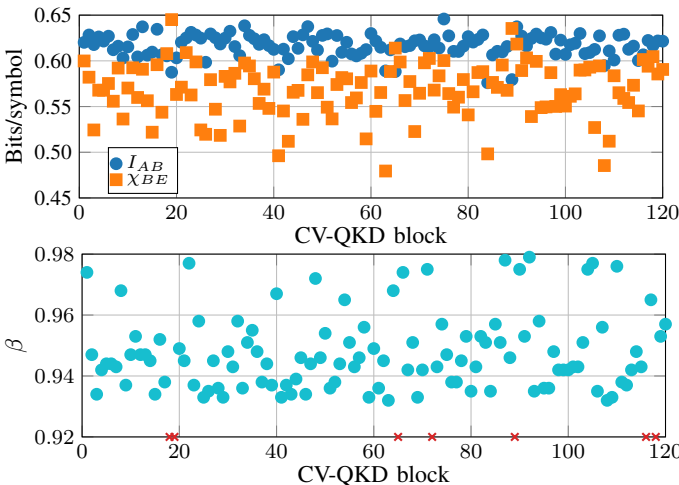


Fig. 10. Experimental results. Top: The I_{AB} and χ_{BE} for 120 CV-QKD blocks for the FSO channel with $\sigma_I = 0.009$ and $\beta_{jitter} = 8.6$. Bottom: The optimal β for each CV-QKD block, using a $R = \frac{1}{5}$ TBP-LDPC code punctured to the $R = \beta I_{AB}$ for each block. The red crosses correspond to the cases where reconciliation is not possible because the SKR is negative regardless of which β is chosen.

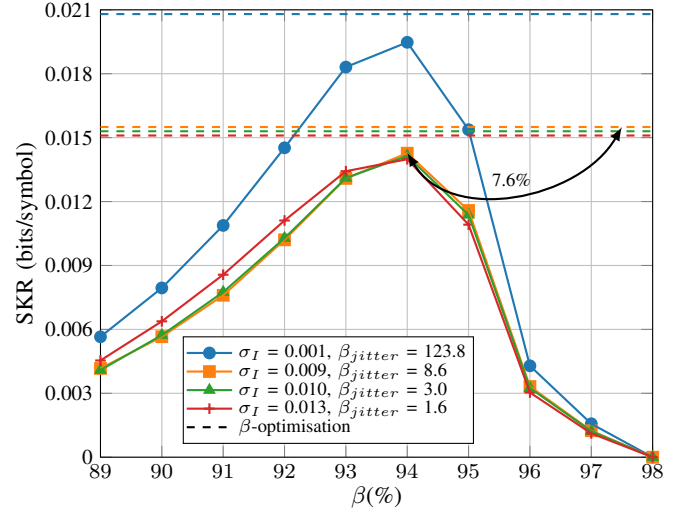


Fig. 11. Experimental Results. β vs. SKR for FSO channels with different turbulence settings. A $R = \frac{1}{5}$ TBP-LDPC code is used, punctured to the appropriate rate. The dashed lines correspond to the SKR when β -optimisation is used.

up to 7.6% are reported. These gains are dependent on both the error correction code used and the stability of the system. The SKR after β -optimisation will always be at least as high as the SKR without β -optimisation, and it is therefore always advantageous to implement it.

VI. CONCLUSION

In this paper, we have investigated the use of high-dimensional reconciliation for CV-QKD. We have analysed how the different modulation formats impact the reconciliation, and using experimental results, we show SKR gains by up to 165%. Furthermore, we have discussed rate-adaptivity for reconciliation in CV-QKD, and have shown that with β -optimisation it is possible to get an additional 7.6% gain in SKR. Future works could focus on efficient implementations of high-dimensional reconciliation in hardware, in addition to a more extensive study on reconciliation in different experimental settings.

REFERENCES

- [1] K. Gümüş, J. d. R. Frazão, V. van Vliet, S. van der Heide, M. v. d. Hout, A. Albores-Mejia, T. Bradley, and C. Okonkwo, "Adaptive Reconciliation for Experimental Continuous-Variable Quantum Key Distribution Over a Turbulent Free-Space Optical Channel," *OFC 2024*, 2024.
- [2] C. H. Bennett and G. Brassard, "Quantum cryptography: Public key distribution and coin tossing," *Theoretical Computer Science*, vol. 560, pp. 7–11, 2014, ISSN: 0304-3975.
- [3] P. W. Shor, "Polynomial-time algorithms for prime factorization and discrete logarithms on a quantum computer," *SIAM review*, vol. 41, no. 2, pp. 303–332, 1999.
- [4] L. Gyongyosi and S. Imre, "A survey on quantum computing technology," *Computer Science Review*, vol. 31, 2019.
- [5] F. Grosshans and P. Grangier, "Continuous variable quantum cryptography using coherent states," *Phys. Rev. Lett.*, vol. 88, p. 057902, 5 2002.
- [6] F. Laudenbach, C. Pacher, C.-H. F. Fung, A. Poppe, M. Peev, B. Schrenk, M. Hentschel, P. Walther, and H. Hübel, "Continuous-variable quantum key distribution with Gaussian modulation—the theory of practical implementations," *Advanced Quantum Technologies*, vol. 1, no. 1, 2018.

- [7] S. Yang, Z. Yan, H. Yang, Q. Lu, Z. Lu, L. Cheng, X. Miao, and Y. Li, "Information reconciliation of continuous-variables quantum key distribution: Principles, implementations and applications," *EPJ Quantum Technology*, vol. 10, no. 1, p. 40, 2023.
- [8] F. Grosshans, G. Van Assche, J. Wenger, R. Brouri, N. J. Cerf, and P. Grangier, "Quantum key distribution using gaussian-modulated coherent states," *Nature*, vol. 421, no. 6920, pp. 238–241, 2003.
- [9] S. Ghorai, P. Grangier, E. Diamanti, and A. Leverrier, "Asymptotic security of continuous-variable quantum key distribution with a discrete modulation," *Physical Review X*, vol. 9, no. 2, p. 021059, 2019.
- [10] E. Kaur, S. Guha, and M. M. Wilde, "Asymptotic security of discrete-modulation protocols for continuous-variable quantum key distribution," *Phys. Rev. A*, vol. 103, p. 012412, 1 2021.
- [11] J. Cho and P. J. Winzer, "Probabilistic constellation shaping for optical fiber communications," *Journal of Lightwave Technology*, vol. 37, no. 6, pp. 1590–1607, 2019.
- [12] A. Denys, P. Brown, and A. Leverrier, "Explicit asymptotic secret key rate of continuous-variable quantum key distribution with an arbitrary modulation," *Quantum*, vol. 5, 2021.
- [13] M. N. Notarnicola, S. Olivares, E. Forestieri, E. Parente, L. Poti, and M. Secondini, "Probabilistic amplitude shaping for continuous-variable quantum key distribution with discrete modulation over a wiretap channel," *IEEE Transactions on Communications*, vol. 72, no. 1, pp. 375–386, 2024, ISSN: 1558-0857.
- [14] A. Leverrier, R. Allé aume, J. Boutros, G. Zémor, and P. Grangier, "Multidimensional reconciliation for a continuous-variable quantum key distribution," *Physical Review A*, vol. 77, no. 4, 2008.
- [15] G. Van Assche, J. Cardinal, and N. Cerf, "Reconciliation of a quantum-distributed gaussian key," *IEEE Transactions on Information Theory*, vol. 50, no. 2, pp. 394–400, 2004.
- [16] P. Jouguet, S. Kunz-Jacques, and A. Leverrier, "Long-distance continuous-variable quantum key distribution with a Gaussian modulation," *Physical Review A*, vol. 84, no. 6, 2011.
- [17] M. Milicevic, C. Feng, L. M. Zhang, and P. G. Gulak, "Quasi-cyclic multi-edge LDPC codes for long-distance quantum cryptography," *npj Quantum Information*, vol. 4, no. 1, 2018.
- [18] C. Zhou, Y. Li, L. Ma, Y. Luo, J. Yang, M. Wu, S. Zhang, W. Huang, and B. Xu, "A high-throughput and FPGA-based LDPC decoder for continuous-variable quantum key distribution system," in *Quantum and Nonlinear Optics X*, Q. He, D.-S. Kim, and C.-F. Li, Eds., International Society for Optics and Photonics, vol. 12775, SPIE, 2023, p. 1 277 517.
- [19] E. E. Cil and L. Schmalen, "An open-source library for information reconciliation in continuous-variable QKD," in *Proc. International Conference on Quantum Cryptography (QCRYPT)*, Vigo, Spain, Sep. 2024.
- [20] X. Wang, Y.-C. Zhang, Z. Li, B. Xu, S. Yu, and H. Guo, "Efficient rate-adaptive reconciliation for continuous-variable quantum key distribution," *arXiv preprint arXiv:1703.04916*, 2017.
- [21] T. A. Eriksson, T. Hirano, B. J. Puttnam, G. Rademacher, R. S. Luís, M. Fujiwara, R. Namiki, Y. Awaji, M. Takeoka, N. Wada, *et al.*, "Wavelength division multiplexing of continuous variable quantum key distribution and 18.3 tbit/s data channels," *Communications Physics*, vol. 2, no. 1, p. 9, 2019.
- [22] A. A. Hajomer, N. Jain, H. Mani, H.-M. Chin, U. L. Andersen, and T. Gehring, "Modulation leakage-free continuous-variable quantum key distribution," *npj Quantum Information*, vol. 8, no. 1, p. 136, 2022.
- [23] Y. Zhang, Z. Chen, S. Pirandola, X. Wang, C. Zhou, B. Chu, Y. Zhao, B. Xu, S. Yu, and H. Guo, "Long-distance continuous-variable quantum key distribution over 202.81 km of fiber," *Physical Review Letters*, vol. 125, no. 1, 2020, ISSN: 1079-7114.
- [24] J. dos Reis Frazão, V. van Vliet, S. van der Heide, M. van den Hout, K. Gümüş, A. Albores-Mejía, B. Škorić, and C. Okonkwo, *Copropagation of Classical and Continuous-variable QKD Signals over a Turbulent Optical Channel with a Real-time QKD Receiver*, Accepted for OFC 2024, 2024. arXiv: 2401.10581 [quant-ph].
- [25] S. Wang, P. Huang, T. Wang, and G. Zeng, "Feasibility of continuous-variable quantum key distribution through fog," *Opt. Lett.*, vol. 46, no. 23, 2021.
- [26] S.-Y. Shen, M.-W. Dai, X.-T. Zheng, Q.-Y. Sun, G.-C. Guo, and Z.-F. Han, "Free-space continuous-variable quantum key distribution of unidimensional Gaussian modulation using polarized coherent states in an urban environment," *Phys. Rev. A*, vol. 100, 1 2019.
- [27] L. E. Dickson, "On quaternions and their generalization and the history of the eight square theorem," *Annals of Mathematics*, pp. 155–171, 1919.
- [28] Y. Zhou, X.-Q. Jiang, W. Liu, T. Wang, P. Huang, and G. Zeng, "Practical security of continuous-variable quantum key distribution under finite-dimensional effect of multi-dimensional reconciliation," *Chinese Physics B*, vol. 27, no. 5, p. 050301, 2018.
- [29] J. Li, A. Bose, and Y. Zhao, "Rayleigh flat fading channels' capacity," in *3rd Annual Communication Networks and Services Research Conference (CNSR'05)*, 2005, pp. 214–217.
- [30] P. Révész, *The laws of large numbers*. Academic Press, 2014, vol. 4.
- [31] A. Leverrier, F. Grosshans, and P. Grangier, "Finite-size analysis of a continuous-variable quantum key distribution," *Physical Review A—Atomic, Molecular, and Optical Physics*, vol. 81, no. 6, p. 062343, 2010.
- [32] T. A. Eriksson, R. S. Luís, K. Gümüş, *et al.*, "Digital self-coherent continuous variable quantum key distribution system," in *Optical Fiber Communication Conference (OFC) 2020*, Optica Publishing Group, 2020, T3D.5. DOI: 10.1364/OFC.2020.T3D.5. [Online]. Available: <https://opg.optica.org/abstract.cfm?URI=OFC-2020-T3D.5>.
- [33] B. Collins and P. Śniady, "Integration with respect to the haar measure on unitary, orthogonal and symplectic group," *Communications in Mathematical Physics*, vol. 264, no. 3, pp. 773–795, 2006.
- [34] A. S. Householder, "Unitary triangularization of a nonsymmetric matrix," *Journal of the ACM (JACM)*, vol. 5, no. 4, pp. 339–342, 1958.
- [35] K. Gümüş and L. Schmalen, "Low rate protograph-based LDPC codes for continuous variable quantum key distribution," *Proc. ISWCS 2021*, 2021.
- [36] X.-Y. Hu, E. Eleftheriou, and D.-M. Arnold, "Regular and irregular progressive edge-growth tanner graphs," *IEEE transactions on information theory*, vol. 51, no. 1, pp. 386–398, 2005.
- [37] M. Beermann and P. Vary, "Joint optimization of multi-rate ldpc code ensembles for the awgn channel based on shortening and puncturing," in *2014 IEEE Wireless Communications and Networking Conference (WCNC)*, 2014, pp. 200–205.
- [38] V. van Vliet, "Optical Turbulence Generator for Lab-based Experimental Studies of Atmospheric Turbulence in Vertical Optical Communication Links," M.S. thesis, TU/e, 2022.
- [39] V. van Vliet, M. van den Hout, S. van der Heide, and C. Okonkwo, "Design, Characterisation, and Demonstration of a Hot-Air-Based Optical Turbulence Generator," in *Proceedings of the 26th Annual Symposium of the IEEE Photonics Benelux Chapter, 26th Annual Symposium of the IEEE Photonics Benelux Chapter*, 2022.
- [40] K. Kiasaleh, "On the probability density function of signal intensity in free-space optical communications systems impaired by pointing jitter and turbulence," *Optical Engineering*, vol. 33, 1994.
- [41] S. van der Heide, J. Frazão, A. Albores-Mejía, and C. Okonkwo, "Receiver noise stability calibration for CV-QKD," *Proc. OFC 2023*, 2023.
- [42] P. Jouguet, S. Kunz-Jacques, E. Diamanti, and A. Leverrier, "Analysis of imperfections in practical continuous-variable quantum key distribution," *Physical Review A*, vol. 86, no. 3, 2012.